PHYSICAL REVIEW A **107**, 063303 (2023)

Two-dimensional miscible-immiscible supersolid and droplet crystal state in a homonuclear dipolar bosonic mixture

Soumyadeep Halder,[*] Subrata Das, and Sonjoy Majumder
Department of Physics, Indian Institute of Technology Kharagpur, Kharagpur 721302, India

(Received 24 January 2023; accepted 16 May 2023; published 8 June 2023)

The recent realization of a binary dipolar Bose-Einstein condensate [A. Trautmann *et al.*, Phys. Rev. Lett. **121**, 213601 (2018)] presents new exciting aspects for studying quantum droplets and supersolids in a binary mixture. Motivated by this experiment, we study the ground-state phases and dynamics of a Dy-Dy mixture. The dipolar bosonic mixture exhibits qualitatively novel and rich physics. Relying on the three-dimensional numerical simulations in the extended Gross-Pitaevskii framework, we unravel the ground-state phase diagrams and characterize their different possible phases. The emergent phases include single-droplet (SD), multiple-droplets (MD), doubly supersolid (SS), and superfluid (SF) states in both miscible and immiscible phases. Intriguing mixed ground states are observed for an imbalanced binary mixture, including a combination of SS-SF, SS-MD, and SS-SS phases. We also explore the dynamics across the phase boundaries by linear quenches of interspecies and intraspecies scattering lengths. During these dynamical processes, we observe an abrupt change in phase which initially results in some instability in the system and forms some metastable states in the intermediate timescale. However, the state produced in long-time evolution is similar to our predicted ground state. Although we demonstrate the possible results for a Dy-Dy mixture and for a specific parameter range of intraspecies and interspecies scattering lengths, our results are in general valid for other dipolar mixtures and may become an important benchmark for future experimental scenarios.

DOI: 10.1103/PhysRevA.107.063303

I. INTRODUCTION

Quantum droplets are dilute liquidlike clusters of atoms produced in a quantum fluid where the dominant attractive mean-field-driven collapse is arrested by the quantum fluctuations [1,2]. The supersolid state is also an intriguing state of matter in which the crystalline order of quantum droplets and a global phase coherence [3,4] coexist as a result of background superfluid. Both of these states were initially predicted and searched for in liquid helium [5–8]. The ability to tune the interaction strength between the particles of an ultracold atomic gas through the Feshbach resonance [9] offers an excellent platform for studying a plethora of rich physical phenomena. In recent years the quest for quantum droplets and supersolid states in ultracold gases has attracted significant attention. Most theoretical and experimental studies over the past few years reveal the formation of droplets, mainly in two different types of ultracold bosonic systems discussed below.

Quantum droplets in ultracold atomic gases were first observed in single-component dipolar bosonic gases with sufficiently large magnetic dipole moments such as dysprosium [10–12] and erbium [13–15]. In this case, when the dipole-dipole interaction (DDI) dominates over the contact interaction in that regime, the anisotropic and long-range characters of the DDI lead to the formation of self-bound quantum droplets [16–22] and supersolid states [23–34]. These droplets with highly anisotropic properties have filamentlike narrow transverse widths and are elongated in the direction of the external magnetic field.

Quantum droplets also have been realized in nondipolar binary homonuclear [35–39] and heteronuclear [40,41] Bose mixtures. Binary mixtures with an attractive interspecies interaction lead to the formation of miscible droplets. Unlike the droplets formed in a single-component dipolar Bose-Einstein condensate (DBEC) due to the anisotropic and partial attractive nature of DDI, these droplets in a binary system originate solely due to the contact interaction and therefore are spherical (isotropic) in nature.

These phases have been widely explored in various ultracold systems and different experimental setups, including rotating dipolar condensates [42–45], DBECs under the influence of a rotating magnetic field [46–49], optical lattice trapped dipolar condensates [50], lattice trapped atomic mixtures [51–53], Rydberg systems [54,55], spin-orbit-coupled systems [56,57], molecular Bose-Einstein condensates (BECs) [58], and a binary mixture of dipolar-nondipolar condensates [59,60].

Recent experimental realization of binary dipolar condensates for the first time [61] and the ability to control their intraspecies and interspecies interaction strengths through the Feshbach resonance [62,63] present new exciting aspects for the study of quantum droplets in a mixture of binary dipolar condensates. Most of the recent theoretical works focus mainly on the formation of a self-bound droplet state in a binary dipolar mixture without any trapping confinement. In contrast to nondipolar

---

[*] soumya.hhs@gmail.com

mixtures, new class of self-bound miscible droplets, and immiscible quantum droplets, forms due to the anisotropic DDI [64–69].

In this article we investigate theoretically the possibility of forming different ground-state phases of a binary DBEC (Dy-Dy mixture) confined in a quasi-two-dimensional harmonic trap. For a balanced system, we observe four different ground-state phases, i.e., doubly superfluid (SF), supersolid (SS), single-droplet (SD), and multiple-droplet (MD) states, that exist in both miscible and immiscible phases. Both components form identical shapes in the miscible phase domain, whereas in the immiscible regime we observe axially immiscible multidomain SD and MD states and asymmetric immiscible doubly SS and SF states. The energetically favored ground state depends on the number of atoms, intra- and intercomponent interactions, and the trap geometry. We depict the phase diagrams and demarcate all these phases. For an imbalanced mixture, more intriguing states, such as a mixture of SS-SF, SS-MD, SF-MD, and SS-SS states, form. We also show that in an immiscible impurity regime, where one of the components consists of a very small number of atoms (minor component), the major component with a larger number of atoms can bind the impurity component in the axial direction and form a self-bound droplet state for a small intraspecies scattering length. However, for comparatively large intra- and interspecies scattering lengths the major component cannot hold the minor component along the axial position. Rather it is pushed in the radially outward direction in the presence of the harmonic trapping potential and forms a radially immiscible mixed state. Using the time-dependent, coupled, extended Gross-Pitaevskii equation (EGPE), we also study the dynamics of a balanced binary system across the above-mentioned phase boundaries.

This paper is structured as follows. Section II describes the theory and formalism, including the coupled EGPE and the overlap integral, to distinguish the miscible and immiscible phases. In Sec. III we extract the phase diagrams of the quasi-two-dimensional dipolar binary BEC. Section IV characterizes different possible ground states for an imbalanced binary mixture. In Sec. V we explore the real-time dynamics and the formation of two-dimensional (2D) miscible-immiscible droplet and supersolid states by using the time-dependent EGPE. A summary of our findings, together with prospects for future work, is provided in Sec. VI. Appendix A describes the components of our numerical simulations. Appendix B is devoted to the variational solution within the same shape approximation (SSA) framework. Appendix C delineates the contrast phase diagrams to differentiate the superfluid, supersolid, and droplet phases. In Appendix D we describe the effective potential experienced by one condensate due to the presence of the other condensate. Finally, in Appendix E we show the time evolution of density profiles and the overlap integral following an interaction quench of a miscible SF state across the relevant phase boundaries.

II. THEORY

We consider a mixture of two species of dipolar bosonic atoms with a large magnetic dipole moment μ_i^m $(i = 1, 2)$ polarized in the z direction by an external magnetic field and confined in a circular symmetric harmonic trapping potential. In the ultracold regime, the atoms of species i are characterized by the macroscopic wave function ψ_i, whose temporal evolution is described by the coupled EGPE

$$i\hbar\frac{\partial\psi_i(\mathbf{r},t)}{\partial t}=\left[-\frac{\hbar^2}{2m_i}\nabla^2+V_t(\mathbf{r})+\sum_{j=1}^{2}\left(g_{ij}|\psi_j(\mathbf{r},t)|^2+\int d\mathbf{r}'V_{ij}^{\rm dd}(\mathbf{r}-\mathbf{r}')|\psi_j(\mathbf{r}',t)|^2\right)+\Delta\mu_i\right]\psi_i(\mathbf{r},t). \qquad (1)$$

Here $V_t(\mathbf{r}) = \frac{1}{2}m_i\omega^2(x^2 + y^2 + \lambda^2 z^2)$ is the harmonic trapping potential with angular frequencies $\omega_x = \omega_y = \omega, \omega_z$; m_i is the atomic mass of the ith species; and $\lambda = \omega_z/\omega$ is the trap aspect ratio. The short-range intra- and intercomponent interaction strengths are given by $g_{ii} = 4\pi\hbar^2 a_{ii}/m_i$ and $g_{ij} = 2\pi\hbar^2 a_{ij}/m_{ij}$, respectively. Here a_{ii} and a_{ij} are the intra- and intercomponent scattering length of atoms and $m_{ij} = m_i m_j/(m_i + m_j)$ is the reduced mass. Apart from the contact interaction, there exists a long-range DDI between the atoms, which takes the form

$$V_{ij}^{\rm dd}(\mathbf{r}) = \frac{3g_{ij}^{\rm dd}}{4\pi}\left(\frac{1-3\cos^2\theta}{r^3}\right), \qquad (2)$$

where $g_{ij}^{\rm dd} = 2\pi\hbar^2 a_{ij}^{\rm dd}/m_{ij}$ is the DDI strength between the atoms of the ith and jth species, with the DDI length $a_{ij}^{\rm dd} = \mu_0\mu_i^m\mu_j^m m_{ij}/6\pi\hbar^2$, and θ is the angle between the axis linking the two particles and the dipole polarization direction (z axis). The last term appearing in Eq. (1) represents the correction to the chemical potential resulting from the effect of quantum fluctuation given by [64,65,68]

$$\Delta\mu_i = \frac{m_i^{3/2}}{3\sqrt{2}\pi^2\hbar^3}\sum_{\pm}\int_0^1 du\,{\rm Re}I_{i\pm}, \qquad (3)$$

where

$$I_{1\pm} = \left(\tilde{U}_{11} \pm \frac{\delta_1\tilde{U}_{11} + 2\tilde{U}_{12}^2 n_2}{\sqrt{\delta_1^2 + 4\tilde{U}_{12}^2 n_1 n_2}}\right)\left(n_1\tilde{U}_{11} + n_2\tilde{U}_{22} \pm \sqrt{\delta_1^2 + 4\tilde{U}_{12}^2 n_1 n_2}\right)^{3/2}, \qquad (4)$$

with $\delta_1 = n_1\tilde{U}_{11} - n_2\tilde{U}_{22}$ and $\tilde{U}_{ij}(u) = g_{ij}[1 + \epsilon_{ij}^{\rm dd}(3u^2 - 1)]$, being the Fourier transform of the total interaction potential and the dimensionless parameter $\epsilon_{ij}^{\rm dd} = a_{ij}^{\rm dd}/a_{ij}$, quantifying the strength of the DDI relative to the contact interaction between the atoms in species i and j. A similar expression for $\Delta\mu_2$ can be easily obtained with $\delta_2 = -\delta_1$. The order parameters of each of the condensates are normalized to the total number of atoms in that species $N_i = \int d\mathbf{r}|\psi_i(\mathbf{r})|^2$.

Overlap integral

A binary DBEC can exhibit a miscible or immiscible phase. A well-known measure to characterize these two phases is the overlap integral, defined as

$$\Lambda = \frac{\left[\int d\mathbf{r}\, n_1(\mathbf{r}) n_2(\mathbf{r})\right]^2}{\left[\int d\mathbf{r}\, n_1^2(\mathbf{r})\right]\left[\int d\mathbf{r} n_2^2(\mathbf{r})\right]}, \tag{5}$$

where $n_i(\mathbf{r}) = |\psi_i(\mathbf{r})|^2$ are the densities of the species i. Here $\Lambda = 1$ implies maximal spatial overlap between the condensates, i.e., the system is in a completely miscible state, whereas a complete phase separation (immiscible phase) corresponds to $\Lambda = 0$.

III. GROUND-STATE PHASES OF A BALANCED MIXTURE

Let us first consider a simplified model of a balanced binary mixture [64,68] consisting of Dy atoms in different spin states,[1] with equal intraspecies interactions[2] ($a_{11} = a_{22}$ and $a_{11}^{\rm dd} = a_{22}^{\rm dd}$) and an equal number of particles in each species ($N_1 = N_2 = N$). Using this model, we explore different possible ground-state phases of a binary DBEC. Ground-state phases of a binary mixture depend on the intra- and interspecies scattering lengths (a_{ii} and a_{12}), the trap aspect ratio λ, and the number of atoms in each species (N). Instead of choosing some arbitrary values of these parameters (a_{ii}, a_{12}, N, and λ), we first evaluate the ground-state phases of the balanced binary dipolar mixture for a broad range of parameters a_{ii}, a_{12}, and N, keeping the trap aspect ratio fixed at $\lambda = 2.95$. Subsequently, we also investigate the effect of trap geometry on the ground-state phases by varying the trap aspect ratio λ with the intraspecies scattering length for a fixed number of particles and interspecies scattering length.

A binary mixture can be in either a miscible or an immiscible phase. We differentiate the miscible and immiscible phases by numerically evaluating the overlap integral Λ [Eq. (5)]. In the large-N limit, the effect of quantum pressure is negligible compared to the nonlinear interactions, and the condensate can be well approximated by the Thomas-Fermi (TF) approximation. Thus immiscibility is completely determined by the intra- and intercomponent scattering lengths for a balanced system [where we can apply the SSA (see Appendix B)] and the transition occurs when $a_{12} = \sqrt{a_{11}a_{22}}$. However, when both condensates consist of a small number of particles, quantum pressure makes a significant contribution to the condition of immiscibility transition. Quantum pressure of individual species is $P_i = \frac{\hbar^2}{2m_i\sqrt{n_i}}\nabla^2\sqrt{n_i}$, where n_i is the density of species i. This pressure describes the attractive force due to spatial variation of density, which becomes maximum at the interface when the two condensates are in an immiscible phase. As a consequence, to minimize the quantum pressure energy for a small number of particles, the miscible to immiscible transition boundary deviates from $a_{12} = \sqrt{a_{11}a_{22}}$ and the binary system favors the miscible state, as can be seen in Figs. 1(a) and 1(b).

Due to the anisotropic DDI, the SF, SS, and droplet (SD and MD) phases emerge in a DBEC. These phases are best characterized by the density contrast $\mathcal{C} = (n_{\max} - n_{\min})/(n_{\max} + n_{\min})$ [60], where $n_{\max}$ and $n_{\min}$ are the neighboring maximum and minimum densities as one moves on the x-y plane (a plane perpendicular to the polarization direction). This allows us to depict different phase domains in the phase diagrams, where we take $\mathcal{C} = 0$ to be a superfluid phase and consider $0 < \mathcal{C} < 0.96$ to be a supersolid and $\mathcal{C} > 0.96$ to be droplet state [60]. For a detailed discussion on the density contrast see Appendix C.

Phase diagrams of a binary dipolar condensate

1. Intraspecies scattering length a_{ii} vs population N

Here we construct a ground-state phase diagram with the intraspecies scattering length a_{ii} ($i = 1, 2$) and the number of particles $N_1 = N_2 = N$ for a constant interspecies scattering length a_{12} [see Fig. 1(a)]. To demonstrate the phase diagram, we fix the interspecies scattering length at $a_{12} = 90a_B$ and vary the intracomponent scattering length a_{ii} from $60a_B$ to $120a_B$ and the number of atoms N from 10^3 to 10^5 of each species. The balanced binary mixture remains in a miscible phase for a large value of a_{ii} ($>a_{12}$). A miscible to immiscible transition for a large number of particles, $N > 4 \times 10^4$, occurs at $a_{ii} = 90a_B$ ($a_{12} = \sqrt{a_{11}a_{22}}$). However, as mentioned above, for $N < 4 \times 10^4$, this transition occurs at smaller a_{ii} ($<90a_B$). This transition is indicated by the white solid line corresponding to $\Lambda = 0.5$ in Fig. 1(a). For sufficiently large a_{ii}, due to the short-range contact-type interactions dominating over the DDI, the binary dipolar mixture remains in a miscible SF state. The mixture corresponds to a smooth (nonmodulated) quasi-2D TF density distribution with a low peak density [similar to Fig. 1(j)]. As we decrease a_{ii} to a critical value, each component of the mixture undergoes an abrupt phase transition to a 2D SS state (overlapping droplets) for a sufficiently large number of particles ($N > 2 \times 10^4$). These droplets are coupled via a low-density superfluid. In this regime, we get two coexisting miscible SS states [Fig. 1(i)] due to $a_{ii} > a_{12}$. In contrast, for a small number of particles $N < 2 \times 10^4$, no droplet nucleation is observed in this regime and both components of the binary mixture remain in a miscible SF state [see Fig. 1(j)]. When further decreasing a_{ii} below $90a_B$, two components become immiscible due to a comparatively large intercomponent scattering length ($a_{12} > a_{ii}$) and the density overlap between the droplets vanishes rapidly. In this sufficiently-low-a_{ii} regime, to minimize the DDI energy, atoms of each species form multiple separate domains in the axial direction and the binary mixture forms a multidomain droplet state. Since we have taken a balanced mixture with equal intra- and interspecies interaction strengths, the binary mixture forms a symmetric immiscible droplet state. For a small number of particles, we observe an immiscible SD state [Fig. 1(c)]. In the case of a sufficiently large number of particles, we obtain an immiscible MD state [Fig. 1(d)].

---

[1] We consider both species to have mass equal to $m = 164$ u. This approximation of equal mass is also valid for any mixture of Dy and Er isotopes. It is important to note that all the bosonic isotopes ^{162}Dy, ^{164}Dy, ^{166}Er, ^{168}Er, and ^{170}Er [61] have a relative mass difference less than 5%.

[2] We take the dipole moment for both components to be $\mu_i^m = 9.93\mu_B$, which corresponds to a dipolar length $a_{ii}^{\rm dd} = 131a_B$ ($i = 1, 2$).

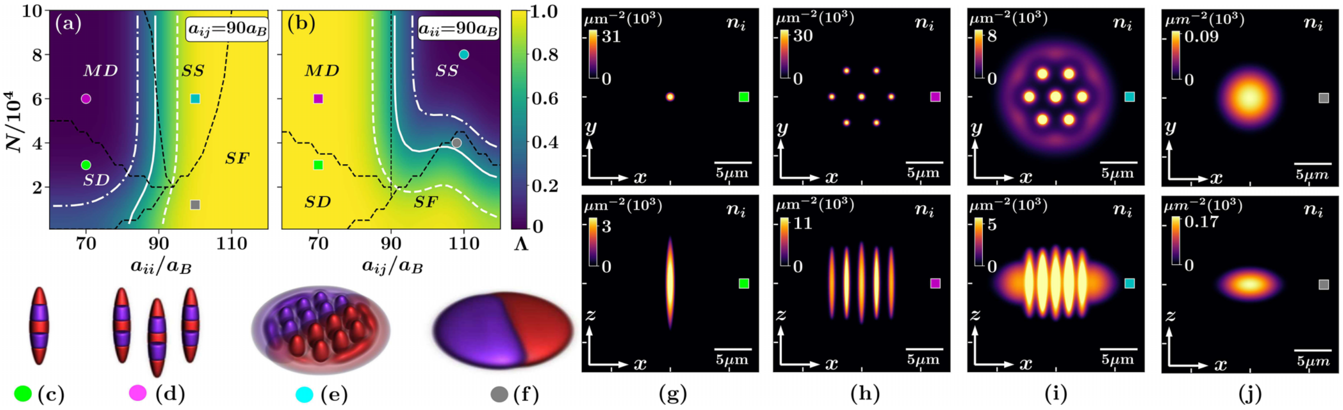

FIG. 1. Ground-state phase diagrams in an oblate harmonic trap of a balanced Dy-Dy mixture as a function of the number of particles and (a) intracomponent and (b) intercomponent s-wave scattering length. The color bar corresponds to the value of the overlap integral Λ. The white solid contour has been drawn at $\Lambda = 0.5$ and indicates the phase transition from a miscible to an immiscible ground state. The two other white dashed and dash-dotted lines are drawn at $\Lambda = 0.9$ and 0.1, respectively. The black dashed lines separate the phase diagram in SF, SS, and single and multiple insulating droplet states. Examples of immiscible 3D isosurfaces of (c) SD (●), (d) MD (●), (e) SS (●), and (f) SF (●) states are shown. Ground-state density profiles of a miscible (g) SD (■), (h) MD (■), and (i) SS (■), and (j) SF (■) states are shown. All these states are highlighted by the corresponding marker in the ground-state phase diagrams [see (a) and (b)]. Here n_i is the density of species i, where $i = 1, 2$ (both the components have identical shapes). Results are for $N_1 = N_2 = N$ and (a) $a_{12} = 90a_B$ and (b) $a_{ii} = 90a_B$, with $a_{ii}^{\mathrm{dd}} = 131a_B$ ($\mu_i^m = 9.93\mu_B$), where a_B is the Bohr radius and $(\omega_x, \omega_y, \omega_z) = 2\pi \times (45, 45, 133)$ Hz.

2. Interspecies scattering length a_{12} vs population N

Now, in the case of a fixed intracomponent scattering length ($a_{ii} = 90a_B$), we construct a ground-state phase diagram [see Fig. 1(b)] by varying the interspecies scattering length a_{12} and the number of atoms N in each species. For a sufficiently large a_{12} ($>80a_B$) and a small number of particles, the stationary state solution of the dipolar mixture is a miscible SF state. The increase in the number of particles N induces a transition to an immiscible SF regime. In this case, since we have taken a balanced mixture, there is no preference for which a particular component remains at the center. So the ground state of the balanced binary mixture has one domain of each species and is separated in the x-y plane, producing an asymmetric immiscible SF state [see Fig. 1(f)]. As we further increase the number of particles ($N > 4 \times 10^4$), the smooth nonmodulated density profile of each domain undergoes a phase transition and each species develops a periodic density modulated pattern on the x-y plane. The density humps (droplets) are connected by lower-density regions (superfluid). Both species exhibit SS properties. However, as we discussed above, in this phase regime, due to large a_{12} ($>a_{ii}$), the phase of the binary mixture is separated in the x-y plane and we obtain an asymmetric immiscible SS state [Fig. 1(e)]. At a lower a_{12} ($<a_{ii}$), the density overlap between the droplets in each species vanishes completely. Furthermore, depending on the number of particles, the binary system displays a miscible SD (small number of particles) and MD (large number of particles) state as portrayed in Figs. 1(g) and 1(h).

3. Intraspecies scattering length vs trap aspect ratio λ

So far, we have discussed the effect of intra- and interspecies contact interactions on the ground state of a binary dipolar mixture for different numbers of atoms. However, the trap aspect ratio $\lambda = \omega_z/\omega$ (trap geometry) is also one of the key parameters to explore different possible ground-state phases. Trap geometry influences the condensate shape as well as the DDI energy. The average DDI energy changes from negative to positive as the shape of the condensate changes from prolate to oblate. To construct a phase diagram with λ and intraspecies scattering length a_{ii} ($i = 1, 2$), we fix the interspecies scattering length at $a_{12} = 90a_B$ and the number of particles at $N_1 = N_2 = 6 \times 10^4$. In Fig. 2 we plot the peak density corresponding to the ground state of a binary mixture as a function of λ and a_{ii}. The peak density results emphasize a significant change in the density among the SF, SS, and droplet (SD and MD) phases (the SS and droplet

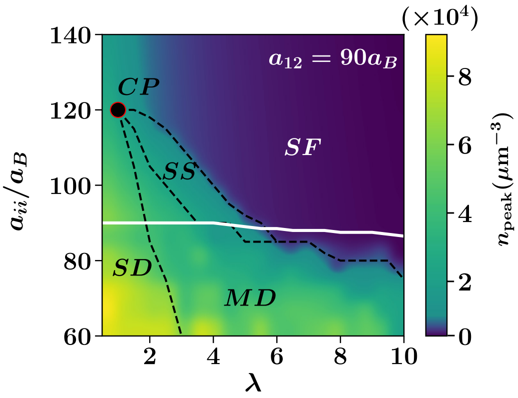

FIG. 2. Ground-state phase diagram of a Dy-Dy mixture as a function of intracomponent s-wave scattering length a_{ii} and trap aspect ratio λ. The shading represents the peak density of the combined binary system. The black dashed lines indicate phase boundaries between the superfluid state (SF) with a low-peak density and a supersolid (SS) and a droplet state (SD and MD) with a high peak density. The black circle with a red border marks the critical point (CP) and the white solid line is drawn at $\Lambda = 0.5$, representing the immiscibility phase boundary. Results are for the case of $N_1 = N_2 = 6 \times 10^4$, ^{164}Dy atoms with $a_{ii}^{\mathrm{dd}} = 131a_B$ ($\mu_i^m = 9.93\mu_B$), where a_B is the Bohr radius and μ_B the Bohr magneton.

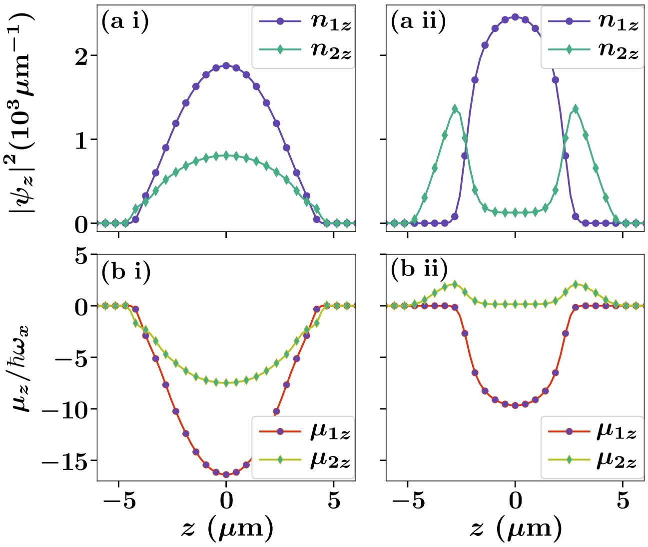

FIG. 3. Miscible and immiscible SD state in an imbalanced mixture. (a) Integrated axial density of species 1 (violet) and species 2 (green) of (a i) a miscible and (a ii) an immiscible SD state. (b) Corresponding chemical potential densities in the axial direction (z axis). Results are for the case of $a_{11} = 70a_B$, $a_{22} = 80a_B$, $N_1 = 10^4$, $N_2 = 5 \times 10^3$, and (a i) and (b i) $a_{12} = 65a_B$ ($<\sqrt{a_{11}a_{22}}$) and (a ii) and (b ii) $a_{12} = 75a_B$ ($>\sqrt{a_{11}a_{22}}$). In both cases the binary mixture is confined in an oblate shape harmonic trap with $(\omega_x, \omega_y, \omega_z) = 2\pi \times (45, 45, 133)$ Hz.

phases are approximately two orders of magnitude denser than the SF phase). All these phase boundaries are shown by black dashed lines. All these phase transition lines terminate at a critical point. Beyond this critical point, there is no abrupt phase transition. Rather a smooth evolution among the abovementioned phases is observed. A similar kind of behavior was also observed for a single-component DBEC [17]. Here the immiscibility boundary is close to $a_{12} = \sqrt{a_{11}a_{22}} = 90a_B$ (as we discussed earlier for a large number of atoms), marked by the white solid line drawn at $\Lambda = 0.5$ in Fig. 2. The regions below ($a_{ii} < a_{12}$) and above ($a_{ii} > a_{12}$) the white solid line correspond to the phase-separated (immiscible) and miscible phase domains, respectively.

IV. SUPERSOLID AND DROPLET STATE IN AN IMBALANCED MIXTURE

Now we consider an imbalanced binary mixture,[3] where the intraspecies interactions and the number of particles among the components are not equal ($a_{11} \neq a_{22}$ and $N_1 \neq N_2$). In addition to all the possible ground states discussed so far, some mixed states such as a mixture of SS-SF, SS-MD, SF-MD, and SS-SS states are formed in this case. Here we consider a Dy-Dy mixture with intraspecies scattering lengths $a_{11} = 70a_B$ and $a_{22} = 80a_B$, and the condensates contain $N_1 = 10^4$ and $N_2 = 5 \times 10^3$ atoms. With these chosen values of parameters, the binary mixture undergoes a miscible SD to immiscible SD phase transition beyond $a_{12} \approx 75a_B$. To look into these miscible and immiscible SD states of the imbalanced mixture, we depict the integrated density profiles n_{1z} and n_{2z} of both species in the axial direction in Figs. 3(a i) and 3(a ii), respectively. In the first scenario with $a_{12} = 65a_B$ ($<\sqrt{a_{11}a_{22}}$), the density profiles of both species completely overlap with each other and form a miscible SD state [see Fig. 3(a i)]. However, as we increase a_{12} beyond the miscible to immiscible transition value, species 1 (major component) remains at the center, due to its larger population (atom number) and smaller intraspecies scattering length. Species 2 (minor component) is pushed in the axial direction and resides at each extreme end of the domain formed by the major component [see Fig. 3(a ii)]. See Appendix D for a discussion of the effective potential experienced by each species due to the presence of the other component.

The reason behind these kinds of density distributions can be clearly understood from the chemical potential densities in the axial direction (μ_z) of each species, as shown in Fig. 3(b). In the miscible SD state, the chemical potential densities of each component are negative, indicating that both components are self-bound. Despite having a different number of particles and intraspecies scattering lengths, the large negative chemical potential of the major component sets the spatial widths of both species equal to each other [see Fig. 3(b i)]. The chemical potential of each species increases with a_{12}. In the immiscible SD and MD regimes, the chemical potential density of the minor component becomes positive. However, due to the negative chemical potential density of the major component in the axial direction, the minor component is bound at each end of the domain formed by the major component [Fig. 3(b ii)].

We show the corresponding 3D isosurface density profile of the immiscible SD state in Fig. 4(a i). In the absence of the major component, the minor component cannot bind itself in these axial positions. The total chemical potential of the binary mixture in this state is still negative, which implies that together they form a self-bound immiscible droplet state.

Mixed ground states can be formed when both condensates of the binary mixture have comparatively large intraspecies scattering lengths and form partially or completely phase-separated (immiscible) ground states. Various ground states of mixed phases such as SS-SF, SS-MD, and SS-SS states form in a binary DBEC depending upon the number of atoms and the intra- and interspecies scattering lengths. The 3D isosurface density profiles of these mixed states are shown in Fig. 4(a). In this regime, beyond a critical value of a_{11} and a_{22} (here we consider $a_{11} < a_{22}$), both components have a slightly positive chemical potential. The species 1 with a smaller intraspecies interaction and a larger number of atoms occupies the central position of the trap, similar to the previous case. However, due to the positive chemical potential, it (the major component) cannot hold the second species at each end along the axial direction. Rather, in the presence of a harmonic trap, the minor component is pushed in the radially outward direction, as illustrated in Figs. 4(a ii)–4(a iv) for the scattering lengths $a_{11} = 90a_B$, $a_{22} = 95a_B$, and $a_{12} = 95a_B$, and species 1 contains $N_1 = 6 \times 10^4$ atoms. For different numbers of atoms in the second species $N_2 = 10^3$, 2×10^4, and 5×10^4 we observe different mixed phases such as SS-SF [Fig. 4(a ii)], SS-MD [Fig. 4(a iii)], and SS-SS phases

---

[3] This imbalanced mixture scenario can arise for any mixture of Dy and Er isotopes or a Er-Dy mixture (suitable for experiments).

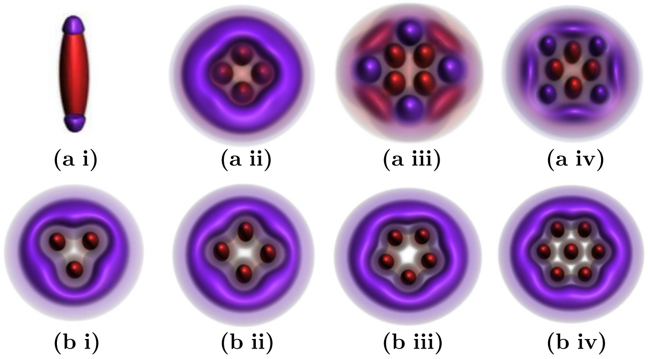

FIG. 4. Three-dimensional isosurface density profiles of [species-1 (red) and species-2 (violet)] immiscible ground states in an imbalanced binary mixture, drawn at 10% of the respective peak densities. (a i) Immiscible SD state in the z direction, with the same parameters as in Fig. 3(a ii). The (a ii) SS-SF, (a iii) SS-MD, and (a iv) SS-SS mixed ground states are shown in the x-y plane. (b) Different pattern formation at the interface of two species in an imbalanced mixture. Results are for the case of a binary DBEC confined in a harmonic trap with $\{\omega_x, \omega_y, \omega_z\} = 2\pi \times \{45, 45, 133\}$ Hz and (a) $a_{11} = 90a_B$, $a_{22} = 95a_B$, $a_{12} = 95a_B$, and $N_1 = 6 \times 10^4$ and (b) $a_{11} = 90a_B$, $a_{22} = 100a_B$, and $a_{12} = 100a_B$. The other parameters are (a ii) $N_2 = 5 \times 10^3$, (a iii) $N_2 = 2 \times 10^4$, (a iv) $N_2 = 5 \times 10^4$, (b i) $N_1 = 6 \times 10^4$ and $N_2 = 10^3$, (b ii) $N_1 = 6 \times 10^4$ and $N_2 = 5 \times 10^3$, (b iii) $N_1 = 8 \times 10^4$ and $N_2 = 1.5 \times 10^4$, and (b iv) $N_1 = 10^5$ and $N_2 = 3 \times 10^4$.

[Fig. 4(a iv)], respectively. The effective potential experienced by each species due to the presence of the other species plays a crucial role in determining the position of the condensates in the trap. In Figs. 5(a) and 5(b) we show the effective potential experienced by each species in the x-y plane for a SS-SF mixed state corresponding to the density profile as shown in Fig. 4(b iv). The corresponding chemical potential densities along the x axis (μ_x) are also shown in Fig. 5(c). As we explained earlier, both condensates have positive chemical potential densities along the x axis [see Fig. 5(c)]. Moreover, the first species experiences a minimum effective potential at the trap center, while the second species finds the same at the periphery of the first condensate and forms a radially immiscible mixture.

Interestingly enough, in a SS-SF mixed state, various polygonal shape patterns form at the interface of the two species depending on the number of droplets in the SS state, as shown in Fig. 4(b). The number of droplets can be varied by changing either the number of atoms or the intraspecies scattering lengths. For the visualization of these polygonal patterns, we choose the intra- and interspecies scattering lengths to be $a_{11} = 90a_B$, $a_{22} = 100a_B$, and $a_{12} = 100a_B$ and the number of atoms (N_1, N_2) to be $(6 \times 10^4, 10^3)$, $(6 \times 10^4, 5 \times 10^3)$, $(8 \times 10^4, 1.5 \times 10^4)$, and $(10^5, 3 \times 10^4)$, which correspond to the triangular [Fig. 4(b i)], rectangular [Fig. 4(b ii)], pentagonal [Fig. 4(b iii)], and hexagonal [Fig. 4(b iv)] shape patterns, respectively, at the interface.

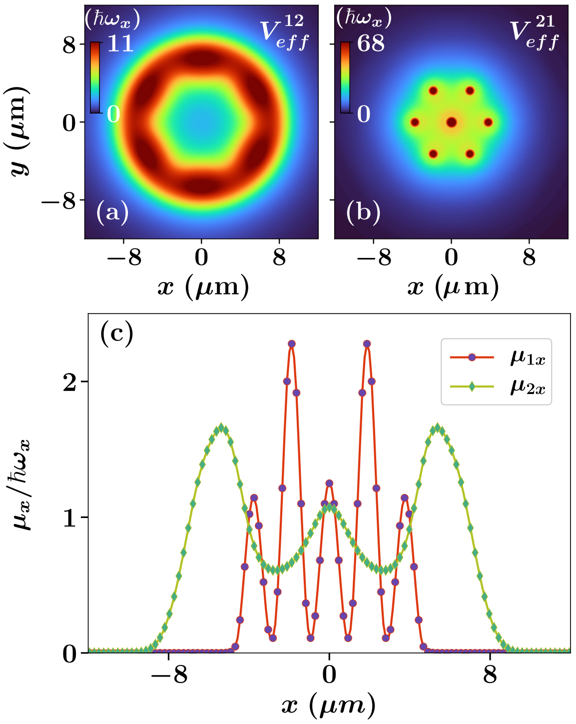

FIG. 5. (a) and (b) Effective potential experienced by the species 1 and specis 2 due to the presence of the other component of a SS-SF mixed state in the $x - y$ plane. The color bar represents the effective potential in units of $\hbar\omega_x$. (c) Corresponding chemical potential densities of species 1 (red) and species 2 (light green) along the x axis. The results are for the case of $a_{11} = 90a_B$, $a_{22} = 100a_B$, $a_{12} = 100a_B$, $N_1 = 10^5$, and $N_2 = 3 \times 10^4$ and the imbalanced binary mixture is confined in a harmonic trap potential with $(\omega_x, \omega_y, \omega_z) = 2\pi \times (45, 45, 133)$ Hz.

V. QUENCH DYNAMICS

So far, we have discussed the phase diagrams of a balanced binary mixture and different possible ground states in an imbalanced binary mixture. Now we explore the effect of quenching intra- and interspecies scattering lengths of a balanced binary mixture in real-time dynamics.

A. Quenching interspecies scattering length

Consider the first case where we initially prepare the DBEC in a miscible MD regime, with $a_{ii} = 90a_B$, $a_{12} = 70a_B$, and $N_1 = N_2 = 6 \times 10^4$. We then perform two different slow linear ramps to increase the value of a_{12}, one from $70a_B$ to $95a_B$ and the other from $70a_B$ to $100a_B$, over a ramp time $t_{\text{on}} = 100$ ms. After that, the interspecies scattering length a_{12} is kept constant to check the stability of the evolved system [see Fig. 6(a)]. We find that both evolutions produce dynamically stable droplets and these results are also consistent with the formation of a self-bound droplet state in a trapless system [65,68]. In Figs. 6(b)–6(f) we show the time evolution of the overlap integral Λ and the density profile of each species in the x-z plane $[n_i(x, z, y = 0)]$, respectively. Initially, while $a_{12} < a_{ii}$, the mixture forms a miscible MD state. During the quenching of the interspecies scattering length, when $a_{12} >$

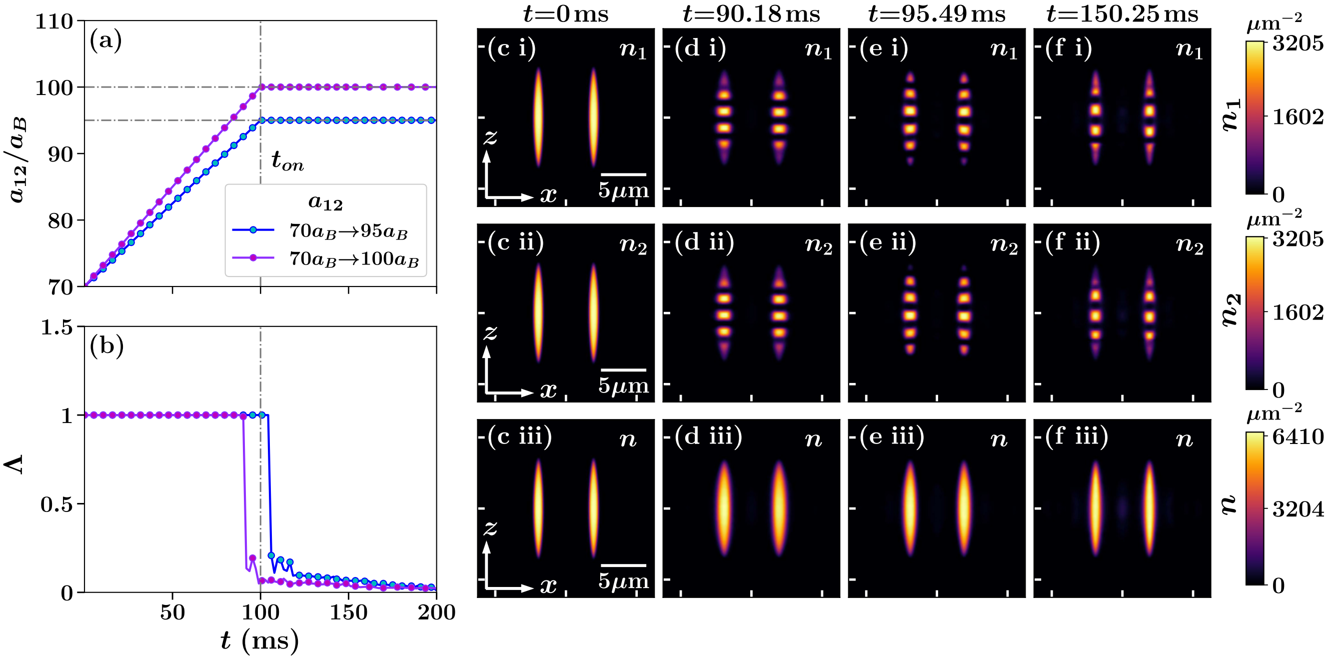

FIG. 6. Tuning the interspecies scattering lengths a_{12} for the fixed values of $a_{ii} = 90a_B$. (a) Linear ramp with ramp time $t_{\rm on} = 100$ ms. From an initial value of $a_{12} = 70a_B$, the interspecies scattering lengths are tuned to the final values $a_{12} = 95a_B$ and $100a_B$, respectively, through this ramp. (b) Corresponding variation of the overlap integral with time. Snapshots of the density profile of (c i)–(f i) species 1 $n_1(x, z, y = 0)$, (c ii)–(f ii) species 2 $n_2(x, z, y = 0)$, and (c iii)–(f iii) the total system $n(x, z, y = 0)$ are shown, following a quench from a miscible MD state with $a_{12} = 70a_B$ to an immiscible MD state with $a_{12} = 100a_B$. Both condensates consist of $N = 6 \times 10^4$ atoms and the balanced binary mixture is confined in a harmonic trap with $(\omega_x, \omega_y, \omega_z) = 2\pi \times (45, 45, 133)$ Hz. The color bar denotes the density in units of μm^{-2}.

a_{ii}, the system rapidly undergoes a miscible to immiscible phase transition. Near the transition time, the value of the overlap integral Λ abruptly changes from 1 to 0 [see Fig. 6(b)]. Due to this sudden change in Λ, the system initially undergoes some instability and forms some metastable states at the intermediate timescale. During this time each component forms multiple periodic segregated domains in the axial direction and forms a completely phase-separated density profile. These extra domains appear as defects due to the discontinuous phase transition. The number of periodic domains decreases with time and the final state produced in long-time evolution is similar to our predicted ground state. In this immiscible state, the density profile of each component is complementary to the other and together they form an axially symmetric immiscible MD state.

B. Quenching intraspecies scattering length

We also explore the dynamical evaluation across the phase boundary by quenching the intraspecies scattering lengths. Here we simulate a procedure to prepare a doubly SS state, starting from a miscible SF state with comparatively large a_{ii}. In this case, the dynamics is triggered by reducing the intraspecies scattering lengths into a miscible and an immiscible SS regime. For a fixed interspecies scattering length at $a_{12} = 90a_B$, we perform two interaction quenches by linearly reducing the intraspecies scattering lengths a_{ii}, one from $120a_B$ to $95a_B$ and the other from $120a_B$ to $85a_B$, over a time period $t_{\rm on} = 100$ ms, after which a_{ii} is held constant [see Fig. 12(a) in Appendix E], and we observe the time evolution of the binary system. In both quenching processes, as a_{ii} is reduced, the system undergoes a roton instability at $a_{ii} \approx 100a_B$. In Fig. 7 we show the time evolution of momentum space density $\tilde{n}(k_x)$, following the quench $a_{ii} = 120a_B$ to $85a_B$. Initially, up to $t = 55.7$ ms, the binary mixture forms a miscible SF state which corresponds to a single density peak at $(k_x, k_y) = (0, 0)\ \mu$m^{-1} [see Fig. 8(a)]. Later following the roton[4] instability at the phase boundary, a ring of radius 3.05 μm^{-1} is readily visible in the k_x-k_y plane and for $k_y = 0$ the density profile $n(k_x, k_y = 0)$ corresponds to the appearance of two additional side peaks in the momentum space (similar to a cigar-shaped trap geometry) [see Fig. 8(b)]. The symmetric side peaks in the momentum space essentially indicate a periodic density modulation in the real space. The binary dipolar mixture forms a miscible SS state in the time interval from $t = 55.7$ ms ($a_{ii} = 100.5a_B$) to $t = 85.7$ ms ($a_{ii} = 90a_B$). As a_{ii} is reduced further the system enters a MD phase domain, and when $a_{ii} < a_{12}$ the overlap integral Λ changes from 1 to 0 rapidly [see Fig. 12(b)] and the system forms an immiscible MD state. The characteristic density snapshots, while performing the quench of a_{ii} from $120a_B$ to $95a_B$, in the $x - y$ plane are presented in Figs. 12(c)–12(e) in Appendix E.

---

[4] The roton modes are characterized by the quantum number m [70–72]. In the $k_x - k_y$ plane, the roton population is spread over a ring which corresponds to a radial roton mode with $m = 0$.

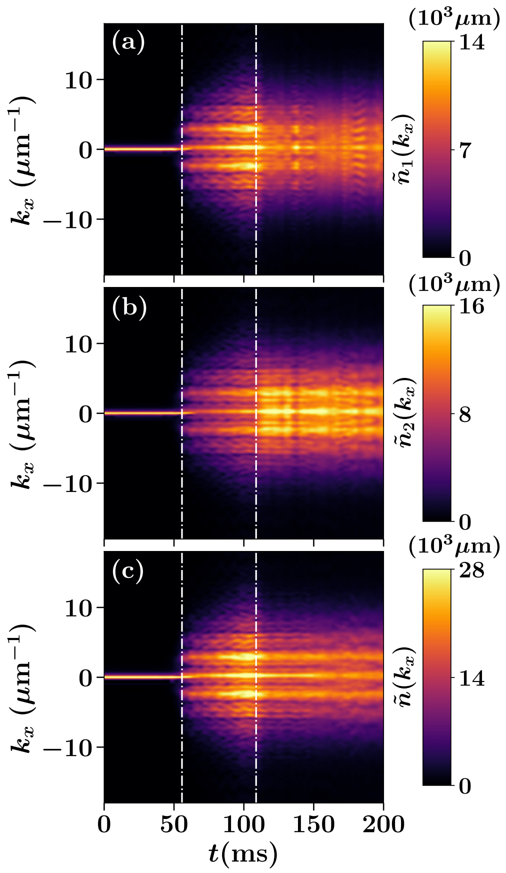

FIG. 7. Time evolution of the momentum space density of (a) species 1 $\tilde{n}_1(k_x)$, (b) species 2 $\tilde{n}_2(k_x)$, and (c) the total system $\tilde{n}(k_x)$, following a linear quench with ramp time $t_{\rm on} = 100$ ms from a miscible SF state with $a_{ii} = 120a_B$ to a immiscible MD state with $a_{ii} = 85a_B$. Both condensates consist of $N = 6 \times 10^4$ atoms, with $a_{12} = 90a_B$, and the balanced binary mixture is confined in a harmonic trap with $(\omega_x, \omega_y, \omega_z) = 2\pi \times (45, 45, 133)$ Hz. The color bar denotes the density in the k_x space, in units of 10^3 μm.

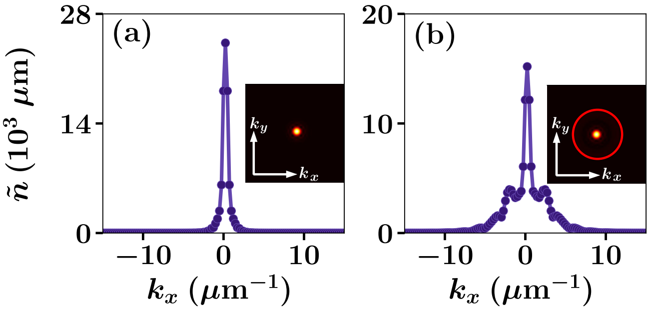

FIG. 8. Snapshots of the density profile of the composite binary system in momentum space following a linear quench with ramp time $t_{\rm on} = 100$ ms from a miscible SF state with $a_{ii} = 120a_B$ to an immiscible MD state with $a_{ii} = 85a_B$, keeping the interspecies scattering length a_{12} fixed at $90a_B$. (a) Initially at $t = 0$ ms, a single peak corresponds to the SF state at $k_x = 0$ μm^{-1}. (b) At $t = 55.7$ ms, two symmetric rotons peak at $k_x = \pm 3.05$ μm^{-1}. The insets show the corresponding density distribution $\tilde{n}(k_x, k_y, k_z{=}0)$ in the $k_x - k_y$ plane. The parameters are the same as in Fig. 7.

VI. CONCLUSION AND OUTLOOK

In this work we have investigated theoretically the scope of formation of two-dimensional supersolid and droplet lattice states in a binary DBEC. We performed an in-depth investigation and demonstrated that a binary dipolar mixture confined in a circular symmetric trap could exhibit a large variety of ground-state phases with rich properties inaccessible for a nondipolar binary mixture and in a single-component DBEC. The emergent phases include SF, SS, SD, and MD states in both miscible and immiscible phase domains. The interplay between intra- and interspecies contact interactions and the anisotropic dipole-dipole interaction leads to the formation of all these phases. Numerically solving the coupled EGPE, we obtained all these results. Besides the 3D numerical simulation, we also employed a variational approach in the SSA framework to validate our results. Although in this work we have demonstrated the results for a Dy-Dy mixture and a specific range of atom-atom interaction strengths, our analysis can be considered as one step forward in the direction of the formation of more exciting new phases in binary dipolar BECs.

We have examined different ground-state phases in a balanced binary DBEC and depicted the phase diagrams as a function of the number of particles and intra- and interspecies scattering lengths. We also monitored the effect of trap geometry in terms of the trap aspect ratio on the ground-state phases. More intriguing mixed phases appear for an imbalanced mixture. In the miscible phase domain, both condensates possess exactly identical shapes, whereas in the immiscible phase domain, we observed two types of immiscible phases: (i) the axially immiscible phase and (ii) the radially immiscible phase. The axially immiscible phase for a self-bound droplet state without any trapping confinement has been predicted in some of the recent theoretical works. However, investigations of the radially immiscible phases are lacking.

In the self-bound immiscible droplet regime, due to the dominant anisotropic dipole-dipole interaction, the component with a larger atom number and smaller intraspecies scattering length takes the central position of the droplet and forms two potential minima at its two outer edges in the axial direction. The second component with a slightly positive chemical potential energy is docked at the above-mentioned position by the first component with a negative chemical potential energy and forms an axially immiscible self-bound droplet state. The chemical potential of each condensate increases with the increase of intra- and interspecies scattering lengths. Hence, in an immiscible regime for a comparatively large value of intraspecies scattering length, the chemical potential of both components becomes positive and the major component can no longer hold the minor component at the axial position. For an imbalanced mixture in the presence of a circularly symmetric harmonic trap, the minor component with a comparatively small number of atoms and large intraspecies scattering length is pushed in the radially outward direction and forms a radially immiscible state. Depending on the value of intraspecies scattering lengths, each species can form a MD, SS, or SF state, whereas for a balanced system, none of the condensates have such bias due to equal interaction strengths and hence forming an asymmetric immiscible state.

Utilizing our ground-state phase diagrams for a balanced binary mixture as a reference, we explored the dynamics across the phase boundaries by tuning the intra- and interspecies interaction strengths. In both processes, we observed an abrupt change in the phase near the transition time. As a consequent of this, the dynamical transition across the phase boundaries initially governed some instability in the system. This led to the formation of some metastable states such as multidomain axially immiscible droplet states and ringlike density structures in the intermediate timescale during the quench-induced dynamics of inter- and intraspecies scattering lengths, respectively. However, as time evolved, the number of extra domains decreased and the ringlike structure broke into multiple density humps (droplets). Thus the state produced in long-time evolution is similar to our predicted ground state.

Our observations pave the way for several future research directions. In this work we restricted our study to a particular Dy-Dy (homonuclear) mixture. However, it would be intriguing to explore the formation of different possible phases in a heteronuclear binary dipolar mixture like the Er-Dy mixture [61–63]. Furthermore, one straightforward option is to investigate the lifetime of these phases by incorporating the effect of three-body interaction loss [15,34]. Another intriguing direction would be to consider the impact of thermal fluctuation and unravel the corresponding phases as well as dynamical nucleation of the supersolid and droplet lattice in the finite-temperature limit [73,74]. Moreover, the evaporation cooling mechanism is an alternative approach to the interaction quench and provides the prospect of forming a long-lived 2D supersolid state in a binary dipolar mixture [24]. Another vital prospect would be to investigate quantum turbulence [75–77], pattern formation [29,78–80], and various topological excitations such as the formation of vortex clusters and solitary waves in a binary dipolar condensate. Finally, the observation discussed in this work would be equally fascinating beyond the Lee-Huang-Yang description [81,82].

ACKNOWLEDGMENTS

We thank Koushik Mukherjee and S. I. Mistakidis for fruitful discussions. S. Halder and S. Das acknowledge MHRD, Govt. of India for the research fellowship. We also acknowledge the National Supercomputing Mission for providing computing resources of PARAM Shakti at IIT Kharagpur, which is implemented by C-DAC and supported by the Ministry of Electronics and Information Technology and Department of Science and Technology, Government of India.

APPENDIX A: NUMERICAL METHODS

Results in this work are based on three-dimensional numerical simulations in the coupled EGPE (1) framework. For the sake of convenience of numerical simulations and better computational precision, we cast the coupled EGPE into a dimensionless form. This is achieved by rescaling the length scale and timescale in terms of the oscillator length $l_{\text{osc}} = \sqrt{\hbar/m\omega_x}$ and trapping frequency ω_x in the x direction. Under this transformation, the wave function of species i obeys $\psi_i(\mathbf{r}') = \sqrt{l_{\text{osc}}^3/N_i}\psi_i(\mathbf{r})$, where N_i is the number of particles in species i. After the transformation of variables into dimensionless quantities, the coupled EGPE is solved by split-step Crank-Nicolson scheme [83]. Since the dipolar potential has a singularity at $r = 0$ [see Eq. (2)], it is numerically evaluated in Fourier space and we obtain the real-space contribution through the application of the convolution theorem. The ground states of binary dipolar condensate are obtained by propagating the relevant equations in imaginary time until the relative deviations of the wave functions (calculated at every grid point) and energy of each condensate between successive time steps are less than 10^{-6} and 10^{-7}, respectively. Furthermore, we fix the normalization of each species at every time instant of the imaginary-time propagation. Using this ground-state solution as an initial state at $t = 0$ and by changing the interaction strengths, we monitor their evolution in real time. Our simulations are performed within a 3D box grid containing 256 × 256 × 256 grid points, with the spatial grid spacing $\Delta_x = \Delta_y = \Delta_z = 0.1 l_{\text{osc}}$ and the time step $\Delta_t = 10^{-4}/\omega_x$.

APPENDIX B: VARIATIONAL SOLUTION WITHIN THE SAME SHAPE APPROXIMATION FRAMEWORK

In addition to numerical 3D simulations of Eq. (1), we employ a simple variational approach in the regime where both components are miscible and take the exact same shape (i.e., $\psi_1 = \psi_2$); this is only possible when both condensates have an equal number of atoms and equal intraspecies interaction. In this regime, the Hamiltonian of the ith condensate is reduced to an effective single-species Hamiltonian given by

$$\begin{aligned}\hat{\mathcal{H}}^i_{\text{SSA}} = &-\frac{\hbar^2}{2m_i}\nabla^2 + V_t(\mathbf{r}) + \mathcal{G}_{\text{SSA}}|\psi_i(\mathbf{r})|^2 \\ &+ \mathcal{G}^{\text{dd}}_{\text{SSA}}\int d\mathbf{r}' U^{\text{dd}}(\mathbf{r}-\mathbf{r}')|\psi_i(\mathbf{r}')|^2 \\ &+ \gamma^{\text{QF}}_{\text{SSA}}\left(\epsilon^{\text{dd}}_{ii}\right)|\psi_i(\mathbf{r})|^3.\end{aligned} \tag{B1}$$

Here $\mathcal{G}_{\text{SSA}} = g_{ii} + g_{12}$ and $\mathcal{G}^{\text{dd}}_{\text{SSA}} = g^{\text{dd}}_{ii} + g^{\text{dd}}_{12}$ are the effective strengths of the contact interaction and DDI, respectively. The last term of Eq. (B1) denotes the contribution of quantum fluctuation. We remark that within this SSA framework, quantum fluctuations depend on the density $n_i^{3/2}$, where $n_i = |\psi_i|^2$. The coefficient of quantum fluctuations $\gamma^{\text{QF}}_{\text{SSA}}$ is well approximated by the known form of a single-species DBEC [84]

$$\begin{aligned}\gamma^{\text{QF}}_{\text{SSA}}\left(\epsilon^{\text{dd}}_{\text{SSA}}\right) = \frac{32}{3}\mathcal{G}_{\text{SSA}}\sqrt{\frac{a^3_{\text{SSA}}}{\pi}}\,\text{Re}\int_0^1 du \\ \times\left[1 + \epsilon^{\text{dd}}_{\text{SSA}}(3u^2 - 1)\right]^{5/2},\end{aligned} \tag{B2}$$

where $a_{\text{SSA}} = a_{ii} + a_{12}$ and the dimensionless parameter $\epsilon^{\text{dd}}_{\text{SSA}} = \mathcal{G}^{\text{dd}}_{\text{SSA}}/\mathcal{G}_{\text{SSA}}$ quantifies the effective relative strength of the DDI to the contact interaction. Within this SSA

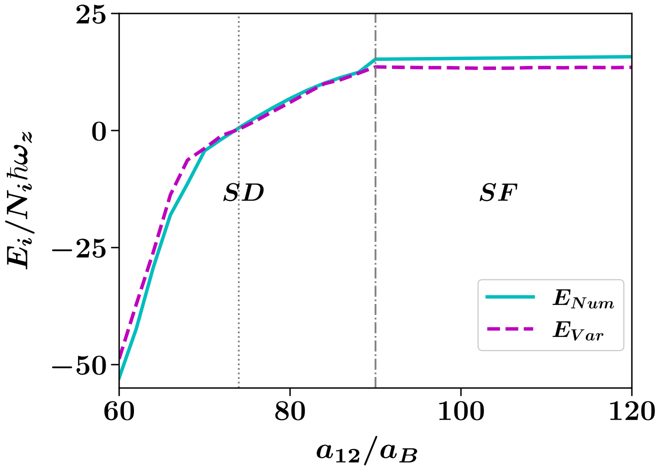

FIG. 9. Variation of energy with the interspecies scattering length a_{12} of a balanced binary mixture. The mixture is confined in a harmonic trap with $(\omega_x, \omega_y, \omega_z) = 2\pi \times (45, 45, 133)$ Hz and the other parameters fixed at $a_{11} = a_{22} = 90a_B$ and $N_1 = N_2 = 10^4$ atoms. The results are obtained through a variational approach within the SSA framework (dashed line) and the coupled EGPE solutions (solid line) are in agreement.

framework, the total energy of the ith species

$$E_i = \int \left(\frac{\hbar^2}{2m_i}|\nabla\psi_i|^2 + V_t(\mathbf{r})|\psi_i(\mathbf{r})|^2 + \frac{\mathcal{G}_{\text{SSA}}}{2}|\psi_i(\mathbf{r})|^4 + \frac{\mathcal{G}^{\text{dd}}_{\text{SSA}}}{2}\int d\mathbf{r}' U^{\text{dd}}(\mathbf{r}-\mathbf{r}')|\psi_i(\mathbf{r}')|^4 + \frac{2}{5}\gamma^{\text{QF}}_{\text{SSA}}|\psi_i(\mathbf{r})|^5 \right) d\mathbf{r}. \tag{B3}$$

A qualitative and to some extent quantitative insight into the droplet and supersolid physics in the miscible SSA regime may be gained from a simplified Gaussian ansatz

$$\psi_i(\mathbf{r}) = \sqrt{\frac{8N_i}{\pi^{3/2}\sigma_\rho^2\sigma_z}} \prod_{\eta=\rho,z} \exp\left(-\frac{2\eta^2}{\sigma_\eta^2}\right), \tag{B4}$$

where the variational parameters are the condensate widths σ_η in the $\eta = \rho, z$ direction. We insert the ansatz (B4) into Eq. (B3) and obtain

$$\frac{E_i}{N_i\hbar\omega_z} = \left(\frac{2l_z^2}{\sigma_\rho^2} + \frac{l_z^2}{\sigma_z^2}\right) + \left(\frac{1}{8\lambda^2}\frac{\sigma_\rho^2}{l_z^2} + \frac{\sigma_z^2}{16l_z^2}\right) + \frac{4N_i\left[\mathcal{G}_{\text{SSA}} - \mathcal{G}^{\text{dd}}_{\text{SSA}} f\left(\frac{\sigma_\rho}{\sigma_z}\right)\right]}{(2\pi)^{3/2}\sigma_\rho^2\sigma_z\hbar\omega_z} + \frac{128N_i^{3/2}\gamma^{\text{QF}}_{\text{SSA}}}{25\sqrt{5}\pi^{9/4}\sigma_\rho^3\sigma_z^{3/2}\hbar\omega_z}, \tag{B5}$$

where

$$f(k) = \frac{1+2k^2}{1-k^2} - \frac{3k^2\tanh^{-1}\sqrt{1-k^2}}{(1-k^2)^{3/2}} \tag{B6}$$

and $l_z = \sqrt{\hbar/m_i\omega_z}$. We find the stationary solutions by numerically locating the values of σ_ρ and σ_z that minimize the variational energy (B5). The energy of a miscible binary mixture obtained through the SSA approach and EGPE solutions are in agreement (see Fig. 9). However, the ansatz (B4) is inappropriate for immiscible and imbalanced droplets and supersolid states (see [64] for an alternative ansatz).

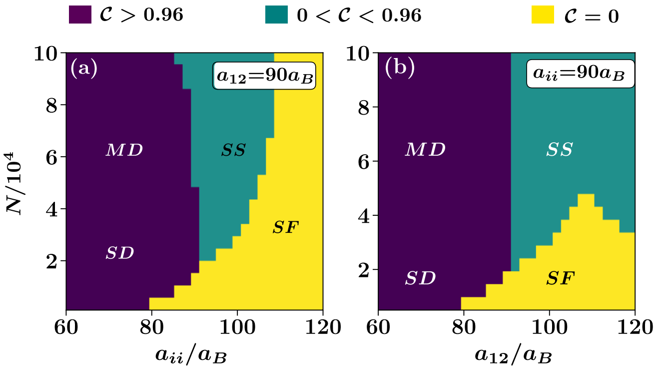

FIG. 10. Ground-state phase diagrams in an oblate harmonic trap of a Dy-Dy mixture as a function of the number of particles in each condensate and (a) intraspecies and (b) interspecies scattering length. The color domains on the phase plots correspond to the different contrast regimes as labeled above the phase diagrams. The other parameters are the same as in Fig. 1.

APPENDIX C: DENSITY CONTRAST

The ground-state phase diagrams for a balanced binary mixture are depicted in Fig. 1. The binary mixture can be in one of the three phases: a SF state, a SS state with periodic density modulation, and a 2D array of isolated droplets. These distinct phases are best characterized by the density contrast, defined as [60]

$$\mathcal{C} = \frac{n_{\text{max}} - n_{\text{min}}}{n_{\text{max}} + n_{\text{min}}}. \tag{C1}$$

Here n_{max} and n_{min} are the neighboring maxima and minima as one moves on the $x - y$ plane. A SF state corresponds to a smooth density distribution with $n_{\text{max}} = n_{\text{min}}$, which implies $\mathcal{C} = 0$. In an insulating droplet state when there is no overlap between the droplets ($n_{\text{min}} \approx 0$), Eq. (C1) gives $\mathcal{C} \approx 1$. However in a SS state, the droplets are connected by a low-density superfluid ($n_{\text{min}} \neq 0$) and the density contrast $\mathcal{C}$ attains an intermediate value between 0 and 1. In this work we consider

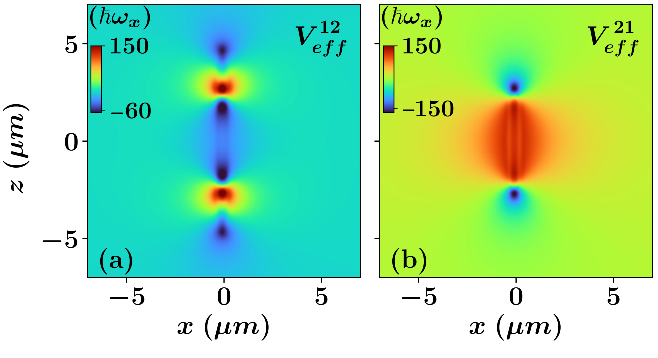

FIG. 11. Effective potential due to the presence of the other component of an immiscible SD state in the $x - z$ plane. The color bar represents the effective potential in units of $\hbar\omega_x$. The other parameters are the same as in Fig. 3(a i).

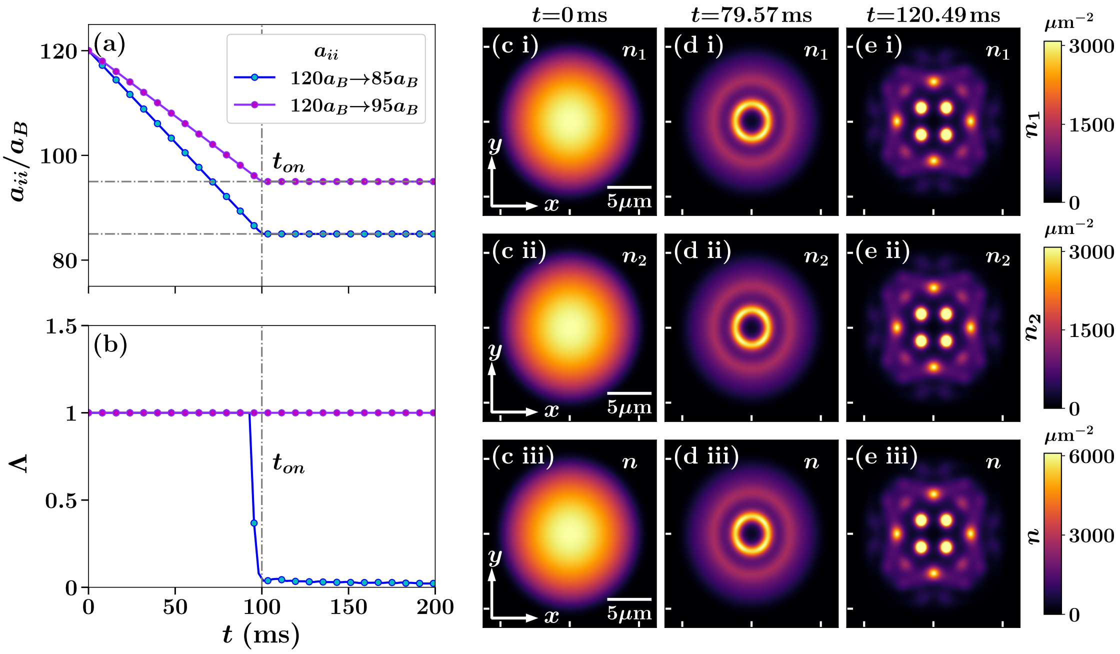

FIG. 12. Quenching intraspecies scattering lengths for a fixed values of $a_{12} = 90a_B$. (a) Linear ramp with ramp time $t_{\rm on} = 100$ ms. From an initial value of $a_{ii} = 120a_B$, the intraspecies scattering lengths are quenched to final values $a_{ii} = 85a_B$ and $95a_B$, respectively, through this ramp. (b) Corresponding variation of the overlap integral with time. Snapshots of the density profile of (c i)–(e i) species 1 $n_1(x, y, z = 0)$, (c ii)–(e ii) species 2 $n_2(x, y, z = 0)$, and (c iii)–(e iii) the total system $n(x, y, z = 0)$ are shown, following a quench from a miscible SF state ($a_{ii} = 120a_B$) to a miscible SS state ($a_{ii} = 95a_B$). Both condensates consist of $N = 6 \times 10^4$ atoms and the balanced binary mixture is confined in a harmonic trap with $(\omega_x, \omega_y, \omega_z) = 2\pi \times (45, 45, 133)$ Hz. The color bar denotes the density in units of μm^{-2}.

[24] $\mathcal{C} = 0$ to be a superfluid phase, $0 < \mathcal{C} < 0.96$ to be a supersolid, and $\mathcal{C} > 0.96$ to be a droplet state. In Fig. 10 we plot the different contrast ($\mathcal{C}$) regimes as a function of intra- and interspecies scattering lengths and the number of particles.

APPENDIX D: EFFECTIVE POTENTIAL

Each condensate experiences an effective potential due to the presence of the other component. The effective potential experienced by species i due to the presence of species j is given by

$$V^{ij}_{\rm eff}(\mathbf{r}) = g_{ij}|\psi_j(\mathbf{r})|^2 + \int d\mathbf{r}' V^{\rm dd}_{ij}(\mathbf{r} - \mathbf{r}')|\psi_j(\mathbf{r}')|^2. \quad \text{(D1)}$$

In the main text, we showed the density profiles of an axially immiscible SD state in an imbalanced binary mixture [see Fig. 3(a ii)]. We observed that the major[5] component with smaller a_{ii} and a larger population acquires the central position and the minor component with larger a_{ii} and a smaller number of atoms is bound at each end in the axial direction. In Fig. 11 we show the corresponding effective potentials experienced by each species due to the presence of other species. Species 1 encounters a minimum potential at the trap center [which is elongated in the axial direction (along the z axis)], whereas the second species experiences a maximum effective potential there but a minimum effective potential at each end of the minimum effective potential domain formed by condensate 1.

APPENDIX E: QUENCH DYNAMICS

To track the emergent features of the intraspecies interaction quench as we discussed in the main text, here we show

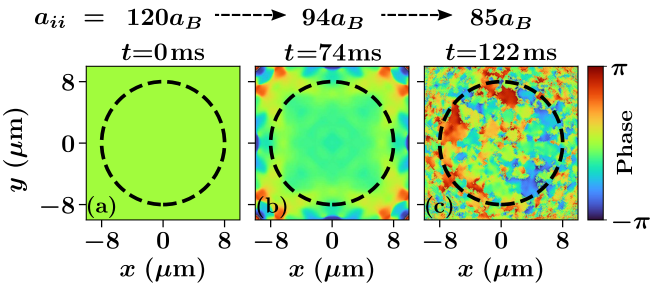

FIG. 13. Characteristic phase profiles of the composite binary mixture in the $x - y$ plane at a specific time instant following a linear quench with ramp time 100 ms from a miscible SF state with $a_{ii} = 120a_B$ to an immiscible MD state with $a_{ii} = 85a_B$, keeping the interspecies scattering length a_{12} fixed at $90a_B$. The black dashed circles delineate the edges of the dipolar binary mixture. The phase profiles correspond to (a) the miscible SF state, (b) the miscible SS state, and (c) the immiscible MD state. The parameters are the same as in Fig. 7.

---

[5] In an imbalanced binary mixture, the species with a larger number of atoms is referred to as the major component and the other species as the minor component.

the time evolution of the density profiles and the phase of the binary mixture. In Fig. 12(a) we show two different interaction quenches of a_{ii}, one from $120a_B$ to $95a_B$ and the other from $120a_B$ to $85a_B$. Following these interaction quenches, the corresponding time evolution of the overlap integral Λ is shown in Fig. 12(b). Initially, at $t = 0$ ms the mixture forms a miscible SF state with a smooth 2D TF distribution [see Fig. 12(c)] which corresponds to a global phase coherence, as can be seen from Fig. 13(a). However, since the quench is performed across the phase boundary, it excites the roton instability in the binary system, leading to ring-shaped density structures, as can be seen in Fig. 12(d). The appearance of the roton mode is readily visible in the momentum space. Due to the circular symmetry of the trap geometry ($\omega_x = \omega_y = \omega$), the roton population is spread over a ring in the k_x-k_y plane and for $k_y = 0$ it corresponds to the appearance of two prominent side peaks, as discussed in the main text [see Fig. 8(b)].

As we decrease the intraspecies scattering lengths more, the ring-shaped density structure breaks into several overlapping density humps (droplets) and the binary mixture forms a miscible SS state [Fig. 12(e)]. This SS state corresponds to an almost perfect global phase coherence with a very small fluctuation in the phase observed due to the interaction quench performed across the phase boundary [see Fig. 13(b)]. Instead of an interaction quench by the evaporative cooling mechanism directly into the SS state, one could produce a SS state with robust global phase coherence as demonstrated in [24]. Further decreasing a_{ii}, the phase coherence between these droplets is completely lost [see Fig. 13(c)] and the binary mixture forms a 2D array of immiscible MD crystals (not shown here).

---

[1] D. S. Petrov, Phys. Rev. Lett. **115**, 155302 (2015).

[2] T. D. Lee, K. Huang, and C. N. Yang, Phys. Rev. **106**, 1135 (1957).

[3] P. Ilzhöfer, M. Sohmen, G. Durastante, C. Politi, A. Trautmann, G. Natale, G. Morpurgo, T. Giamarchi, L. Chomaz, M. J. Mark, and F. Ferlaino, Nat. Phys. **17**, 356 (2021).

[4] L. Tanzi, E. Lucioni, F. Famà, J. Catani, A. Fioretti, C. Gabbanini, R. N. Bisset, L. Santos, and G. Modugno, Phys. Rev. Lett. **122**, 130405 (2019).

[5] J. P. Toennies, A. F. Vilesov, and K. B. Whaley, Phys. Today **54**(2), 31 (2001).

[6] J. P. Toennies and A. F. Vilesov, Angew. Chem. Int. Ed. **43**, 2622 (2004).

[7] M. Barranco, R. Guardiola, S. Hernández, R. Mayol, J. Navarro, and M. Pi, J. Low Temp. Phys. **142**, 1 (2006).

[8] F. Ancilotto, M. Barranco, F. Coppens, J. Eloranta, N. Halberstadt, A. Hernando, D. Mateo, and M. Pi, Int. Rev. Phys. Chem. **36**, 621 (2017).

[9] C. Chin, R. Grimm, P. Julienne, and E. Tiesinga, Rev. Mod. Phys. **82**, 1225 (2010).

[10] H. Kadau, M. Schmitt, M. Wenzel, C. Wink, T. Maier, I. Ferrier-Barbut, and T. Pfau, Nature (London) **530**, 194 (2016).

[11] F. Wächtler and L. Santos, Phys. Rev. A **94**, 043618 (2016).

[12] I. Ferrier-Barbut, H. Kadau, M. Schmitt, M. Wenzel, and T. Pfau, Phys. Rev. Lett. **116**, 215301 (2016).

[13] L. Chomaz, Phys. Rev. X **6**, 041039 (2016).

[14] D. Petter, G. Natale, R. M. W. van Bijnen, A. Patscheider, M. J. Mark, L. Chomaz, and F. Ferlaino, Phys. Rev. Lett. **122**, 183401 (2019).

[15] L. Chomaz, D. Petter, P. Ilzhöfer, G. Natale, A. Trautmann, C. Politi, G. Durastante, R. M. W. van Bijnen, A. Patscheider, M. Sohmen, M. J. Mark, and F. Ferlaino, Phys. Rev. X **9**, 021012 (2019).

[16] M. Schmitt, M. Wenzel, F. Böttcher, I. Ferrier-Barbut, and T. Pfau, Nature (London) **539**, 259 (2016).

[17] R. N. Bisset, R. M. Wilson, D. Baillie, and P. B. Blakie, Phys. Rev. A **94**, 033619 (2016).

[18] D. Baillie, R. M. Wilson, and P. B. Blakie, Phys. Rev. Lett. **119**, 255302 (2017).

[19] F. Cinti and M. Boninsegni, Phys. Rev. A **96**, 013627 (2017).

[20] D. Baillie and P. B. Blakie, Phys. Rev. Lett. **121**, 195301 (2018).

[21] A.-C. Lee, D. Baillie, and P. B. Blakie, Phys. Rev. Res. **3**, 013283 (2021).

[22] F. Wächtler and L. Santos, Phys. Rev. A **93**, 061603(R) (2016).

[23] M. A. Norcia, C. Politi, L. Klaus, E. Poli, M. Sohmen, M. J. Mark, R. N. Bisset, L. Santos, and F. Ferlaino, Nature (London) **596**, 357 (2021).

[24] T. Bland, E. Poli, C. Politi, L. Klaus, M. A. Norcia, F. Ferlaino, L. Santos, and R. N. Bisset, Phys. Rev. Lett. **128**, 195302 (2022).

[25] Y.-C. Zhang, F. Maucher, and T. Pohl, Phys. Rev. Lett. **123**, 015301 (2019).

[26] S. M. Roccuzzo and F. Ancilotto, Phys. Rev. A **99**, 041601(R) (2019).

[27] E. Poli, T. Bland, C. Politi, L. Klaus, M. A. Norcia, F. Ferlaino, R. N. Bisset, and L. Santos, Phys. Rev. A **104**, 063307 (2021).

[28] G. Natale, R. M. W. van Bijnen, A. Patscheider, D. Petter, M. J. Mark, L. Chomaz, and F. Ferlaino, Phys. Rev. Lett. **123**, 050402 (2019).

[29] J. Hertkorn, J.-N. Schmidt, M. Guo, F. Böttcher, K. S. H. Ng, S. D. Graham, P. Uerlings, T. Langen, M. Zwierlein, and T. Pfau, Phys. Rev. Res. **3**, 033125 (2021).

[30] M. Sohmen, C. Politi, L. Klaus, L. Chomaz, M. J. Mark, M. A. Norcia, and F. Ferlaino, Phys. Rev. Lett. **126**, 233401 (2021).

[31] J. Léonard, A. Morales, P. Zupancic, T. Esslinger, and T. Donner, Nature (London) **543**, 87 (2017).

[32] L. Tanzi, S. M. Roccuzzo, E. Lucioni, F. Famà, A. Fioretti, C. Gabbanini, G. Modugno, A. Recati, and S. Stringari, Nature (London) **574**, 382 (2019).

[33] M. Guo, F. Böttcher, J. Hertkorn, J.-N. Schmidt, M. Wenzel, H. P. Büchler, T. Langen, and T. Pfau, Nature (London) **574**, 386 (2019).

[34] F. Böttcher, J.-N. Schmidt, M. Wenzel, J. Hertkorn, M. Guo, T. Langen, and T. Pfau, Phys. Rev. X **9**, 011051 (2019).

[35] C. R. Cabrera, L. Tanzi, J. Sanz, B. Naylor, P. Thomas, P. Cheiney, and L. Tarruell, Science **359**, 301 (2018).

[36] G. Semeghini, G. Ferioli, L. Masi, C. Mazzinghi, L. Wolswijk, F. Minardi, M. Modugno, G. Modugno, M. Inguscio, and M. Fattori, Phys. Rev. Lett. **120**, 235301 (2018).

[37] P. Cheiney, C. R. Cabrera, J. Sanz, B. Naylor, L. Tanzi, and L. Tarruell, Phys. Rev. Lett. **120**, 135301 (2018).
[38] G. Ferioli, G. Semeghini, L. Masi, G. Giusti, G. Modugno, M. Inguscio, A. Gallemí, A. Recati, and M. Fattori, Phys. Rev. Lett. **122**, 090401 (2019).
[39] T. A. Flynn, L. Parisi, T. P. Billam, and N. G. Parker, Quantum droplets in imbalanced atomic mixtures, arXiv:2209.04318 .
[40] Z. Guo, F. Jia, L. Li, Y. Ma, J. M. Hutson, X. Cui, and D. Wang, Phys. Rev. Res. **3**, 033247 (2021).
[41] C. D'Errico, A. Burchianti, M. Prevedelli, L. Salasnich, F. Ancilotto, M. Modugno, F. Minardi, and C. Fort, Phys. Rev. Res. **1**, 033155 (2019).
[42] X.-F. Zhang, L. Wen, C.-Q. Dai, R.-F. Dong, H.-F. Jiang, H. Chang, and S.-G. Zhang, Sci. Rep. **6**, 19380 (2016).
[43] S. M. Roccuzzo, A. Gallemí, A. Recati, and S. Stringari, Phys. Rev. Lett. **124**, 045702 (2020).
[44] A. Gallemí, S. M. Roccuzzo, S. Stringari, and A. Recati, Phys. Rev. A **102**, 023322 (2020).
[45] L. Klaus, T. Bland, E. Poli, C. Politi, G. Lamporesi, E. Casotti, R. N. Bisset, M. J. Mark, and F. Ferlaino, Nat. Phys. **18**, 1453 (2022).
[46] S. B. Prasad, T. Bland, B. C. Mulkerin, N. G. Parker, and A. M. Martin, Phys. Rev. Lett. **122**, 050401 (2019).
[47] D. Baillie and P. B. Blakie, Phys. Rev. A **101**, 043606 (2020).
[48] S. B. Prasad, B. C. Mulkerin, and A. M. Martin, Phys. Rev. A **103**, 033322 (2021).
[49] S. Halder, K. Mukherjee, S. I. Mistakidis, S. Das, P. G. Kevrekidis, P. K. Panigrahi, S. Majumder, and H. R. Sadeghpour, Phys. Rev. Res. **4**, 043124 (2022).
[50] J. Zhang, C. Zhang, J. Yang, and B. Capogrosso-Sansone, Phys. Rev. A **105**, 063302 (2022).
[51] D. Heidarian and A. Paramekanti, Phys. Rev. Lett. **104**, 015301 (2010).
[52] K. Suthar, H. Sable, R. Bai, S. Bandyopadhyay, S. Pal, and D. Angom, Phys. Rev. A **102**, 013320 (2020).
[53] F. Hébert, G. G. Batrouni, X. Roy, and V. G. Rousseau, Phys. Rev. B **78**, 184505 (2008).
[54] F. Cinti, P. Jain, M. Boninsegni, A. Micheli, P. Zoller, and G. Pupillo, Phys. Rev. Lett. **105**, 135301 (2010).
[55] N. Henkel, F. Cinti, P. Jain, G. Pupillo, and T. Pohl, Phys. Rev. Lett. **108**, 265301 (2012).
[56] J.-R. Li, J. Lee, W. Huang, S. Burchesky, B. Shteynas, F. Ç. Top, A. O. Jamison, and W. Ketterle, Nature (London) **543**, 91 (2017).
[57] R. Sachdeva, M. N. Tengstrand, and S. M. Reimann, Phys. Rev. A **102**, 043304 (2020).
[58] M. Schmidt, L. Lassablière, G. Quéméner, and T. Langen, Phys. Rev. Res. **4**, 013235 (2022).
[59] S. Li, U. N. Le, and H. Saito, Phys. Rev. A **105**, L061302 (2022).
[60] T. Bland, E. Poli, L. A. P. Ardila, L. Santos, F. Ferlaino, and R. N. Bisset, Phys. Rev. A **106**, 053322 (2022).
[61] A. Trautmann, P. Ilzhöfer, G. Durastante, C. Politi, M. Sohmen, M. J. Mark, and F. Ferlaino, Phys. Rev. Lett. **121**, 213601 (2018).
[62] G. Durastante, C. Politi, M. Sohmen, P. Ilzhöfer, M. J. Mark, M. A. Norcia, and F. Ferlaino, Phys. Rev. A **102**, 033330 (2020).
[63] C. Politi, A. Trautmann, P. Ilzhöfer, G. Durastante, M. J. Mark, M. Modugno, and F. Ferlaino, Phys. Rev. A **105**, 023304 (2022).
[64] R. N. Bisset, L. A. P. Ardila, and L. Santos, Phys. Rev. Lett. **126**, 025301 (2021).
[65] J. C. Smith, P. B. Blakie, and D. Baillie, Phys. Rev. A **104**, 053316 (2021).
[66] A.-C. Lee, D. Baillie, and P. B. Blakie, Phys. Rev. Res. **4**, 033153 (2022).
[67] A.-C. Lee, D. Baillie, P. B. Blakie, and R. N. Bisset, Phys. Rev. A **103**, 063301 (2021).
[68] J. C. Smith, D. Baillie, and P. B. Blakie, Phys. Rev. Lett. **126**, 025302 (2021).
[69] D. Scheiermann, L. A. P. Ardila, T. Bland, R. N. Bisset, and L. Santos, Phys. Rev. A **107**, L021302 (2023).
[70] J.-N. Schmidt, J. Hertkorn, M. Guo, F. Böttcher, M. Schmidt, K. S. H. Ng, S. D. Graham, T. Langen, M. Zwierlein, and T. Pfau, Phys. Rev. Lett. **126**, 193002 (2021).
[71] J. Hertkorn, J.-N. Schmidt, M. Guo, F. Böttcher, K. S. H. Ng, S. D. Graham, P. Uerlings, H. P. Büchler, T. Langen, M. Zwierlein, and T. Pfau, Phys. Rev. Lett. **127**, 155301 (2021).
[72] L. Chomaz, R. M. W. van Bijnen, D. Petter, G. Faraoni, S. Baier, J. H. Becher, M. J. Mark, F. Wächtler, L. Santos, and F. Ferlaino, Nat. Phys. **14**, 442 (2018).
[73] J. Sánchez-Baena, C. Politi, F. Maucher, F. Ferlaino, and T. Pohl, Nat. Commun. **14**, 1868 (2023).
[74] G. De Rosi, G. E. Astrakharchik, and P. Massignan, Phys. Rev. A **103**, 043316 (2021).
[75] S. P. Johnstone, A. J. Groszek, P. T. Starkey, C. J. Billington, T. P. Simula, and K. Helmerson, Science **364**, 1267 (2019).
[76] G. Gauthier, M. T. Reeves, X. Yu, A. S. Bradley, M. A. Baker, T. A. Bell, H. Rubinsztein-Dunlop, M. J. Davis, and T. W. Neely, Science **364**, 1264 (2019).
[77] S. Das, K. Mukherjee, and S. Majumder, Phys. Rev. A **106**, 023306 (2022).
[78] Y.-C. Zhang, T. Pohl, and F. Maucher, Phys. Rev. A **104**, 013310 (2021).
[79] D. K. Maity, K. Mukherjee, S. I. Mistakidis, S. Das, P. G. Kevrekidis, S. Majumder, and P. Schmelcher, Phys. Rev. A **102**, 033320 (2020).
[80] K. Kwon, K. Mukherjee, S. J. Huh, K. Kim, S. I. Mistakidis, D. K. Maity, P. G. Kevrekidis, S. Majumder, P. Schmelcher, and J.-y. Choi, Phys. Rev. Lett. **127**, 113001 (2021).
[81] M. Ota and G. Astrakharchik, SciPost Phys. **9**, 020 (2020).
[82] H. Hu and X.-J. Liu, Phys. Rev. Lett. **125**, 195302 (2020).
[83] J. Crank and P. Nicolson, Math. Proc. Cambridge **43**, 50 (1947).
[84] A. R. P. Lima and A. Pelster, Phys. Rev. A **84**, 041604(R) (2011).